Anisotropic Rashba effect and charge and spin currents in monolayer BiTeI by controlling symmetry

Shi-Hao Zhang and Bang-Gui Liu*

Beijing National Laboratory for Condensed Matter Physics, Institute of Physics, Chinese Academy of Sciences, Beijing 100190, China and School of Physical Sciences, University of Chinese Academy of Sciences, Beijing 100190, China

(Received 17 September 2019; revised manuscript received 15 October 2019; published 30 October 2019)

The manipulation of Rashba effects in two-dimensional (2D) electron systems in semiconductors is highly desirable for controllable electronic and optical applications. Here, combining a first-principles investigation and model analysis, we use uniaxial stress to control monolayer BiTeI as a Rashba 2D semiconductor. We find that the stress-driven electron system can be described by an effective anisotropic Rashba model including all three Pauli matrices, and uniaxial stress allows an out-of-plane spin component because of rotational symmetry breaking. When appropriate electron carriers are introduced into the monolayer, an in-plane electric field can induce a charge current and three spin current components (including that based on the out-of-plane spin) because of the reduced symmetry. Therefore, uniaxial stress can be used to control Rashba 2D electron systems such as monolayer BiTeI for promising spintronic devices.

DOI: 10.1103/PhysRevB.100.165429

I. INTRODUCTION

Since the advent of graphene, it becomes clear that two-dimensional (2D) materials can be used to realize high-performance devices for next-generation electronic and optical applications. Various important electronic, magnetic, optical, and mechanical phenomena and effects have been observed. As an important effect, the Rashba effect is a spin splitting phenomenon, originating from the spin-orbit coupling (SOC) in electronic systems without out-of-plane mirror symmetry [1–3]. In a 2D electron gas system, this phenomenon can be described by the famous Rashba model [4,5]. The energy bands of this two-band model have a crossing point at the Γ point. The extremum of the two bands is located along a circle of radius k_0 around the Γ point, and the energy difference between the extremum and the crossing point is defined as the Rashba splitting energy $\mathcal{E}_R$ [3]. It has been proved through first-principles and experimental investigations that there exist strong Rashba effects in some monolayers, multilayers, and heterostructures, such as Janus transition-metal dichalcogenide monolayers [6], monolayer BiSb [7–9], PbX monolayers (X = S, Se, Te) [10,11], monolayer Ag_2Te [12], gated multilayer InSe [13], and GaX/MoX_2 (X = S, Se, Te) heterostructures [14]. The bulk BiTeI, as a polar crystal with a layered crystal structure, has attracted more and more attention because of the strong Rashba splitting [15–24], optical response [25,26], and topological physics [27–30]. The monolayer BiTeI was also predicted to be a polar material with a giant Rashba effect [31,32]. Recently, monolayer BiTeI was experimentally realized [33]. It is highly desirable to manipulate the monolayer BiTeI by applying uniaxial stress in order to use the full potential of the monolayer BiTeI for controlling the Rashba effects and seeking promising charge/spin currents.

Here, we use uniaxial stress to manipulate the monolayer BiTeI semiconductor through combining first-principles investigations and theoretical model analyses. Our first-principles results reveal that uniaxial stress can cause rotational symmetry breaking and strong anisotropy in the energy bands (especially near the Γ point), and make a remarkable out-of-plane spin component occur. We obtain an effective two-band Hamiltonian to describe well the stress-dependent conduction bands and spin texture. After introducing electron carriers of low concentration, an in-plane electric field can induce a charge current and three nonzero spin current components, including an out-of-plane spin current component, in the monolayer because of the broken inversion symmetry. Controllable anisotropic Rashba effects and charge and spin currents can be realized in this way. More detailed results will be presented in the following.

II. METHODOLOGY

The first-principles calculations are performed with the projector augmented-wave (PAW) method within the density functional theory [34], as implemented in the Vienna *ab initio* simulation package software (VASP) [35]. The kinetic energy cutoff of the plane waves is set to 400 eV. All atomic positions are fully optimized until the energy difference between two successive steps is smaller than 10^{-6} eV and the Hellmann-Feynman forces on each atom are less than 0.01 eV/Å. The generalized gradient approximation (GGA) by Perdew, Burke, and Ernzerhof (PBE) [36] is used as the exchange-correlation functional. The Brillouin zone integration in the self-consistent calculation is carried out with a 42×28×1 special Γ-centered k-point mesh following the convention of Monkhorst-Pack [37]. The spin-orbit coupling (SOC) effect is taken into consideration in all calculations including structure optimizations, self-consistent calculations, and energy-band calculations. In order to calculate the Rashba coefficients, we take 1001 k points along each high-symmetry line in the

*bgliu@iphy.ac.cn

 ©2019 American Physical Society

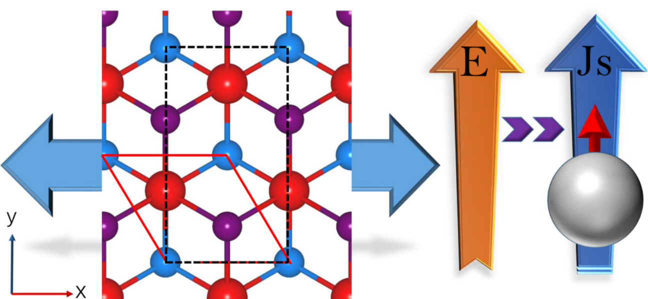

FIG. 1. The crystal structure of monolayer BiTeI and an illustration of the uniaxial stress. The red, blue, and purple balls refer to the bismuth, tellurium, and iodine atoms, respectively. When applying on the stretched monolayer, the in-plane electric field **E** can cause the spin current J_s shown.

energy-band calculations to avoid the errors coming from the discreteness of the k points and ensure the convergence of the Rashba parameter along different directions.

III. RESULT AND DISCUSSION

A. Uniaxial stress and anisotropic Rashba effects

The structure of monolayer BiTeI, without external stress, is presented in Fig. 1. The red solid line represents the unit cell of monolayer BiTeI. It obeys the $P3m1$ space group and shows C_{3v} symmetry. The calculated lattice parameter of monolayer BiTeI is 4.430 Å, which is in agreement with a previous theoretical study (4.422 Å) [38]. For convenience, we take the rectangular cell marked by the black dashed line to calculate the effects of uniaxial stress. Through applying the uniaxial tensile stress upon the monolayer along the x (or y) direction, the C_{3v} symmetry will be removed and the monolayer keeps the M_x mirror symmetry only, and substantial structural anisotropy appears between the x and y directions. When a tensile uniaxial stress is along the x (y) axis, there will be a tensile strain along the x (y) axis and a compressive strain along the y (x) axis due to the Poisson effect. Actually, we allow the tensile x (y) strain to change actively and determine the compressive y (x) strain by structural optimization, and then we estimate the tensile x (y) stress by $\partial\mathcal{E}/A\partial\eta$ where $\mathcal{E}$ is the total energy of the monolayer under η strain along the x (y) direction and A is the area of the stretched unit cell. Our study shows that the 10% tensile strain along the x or y axis can be achieved by applying 1.71 or 1.82 N/m as the uniaxial stress along the same axis, which indicates that the uniaxial stress on monolayer BiTeI is experimentally accessible.

The effect of uniaxial stress on the energy bands of monolayer BiTeI is shown in Fig. 2(a), where the left part describes the bands without stress, the middle part those for 10% tensile strain (stress 1.71 N/m) along the x axis, and the right part those for 10% tensile strain (stress 1.82 N/m) along the y axis. When no stress is applied on the monolayer, the conduction bands near the Γ point behave isotropically, and the calculated Rashba parameters ($\mathcal{E}_R$, k_0, and α) are 38.4 meV, 0.042 Å^{-1}, and 1.82 eV Å, in agreement with a previous theoretical

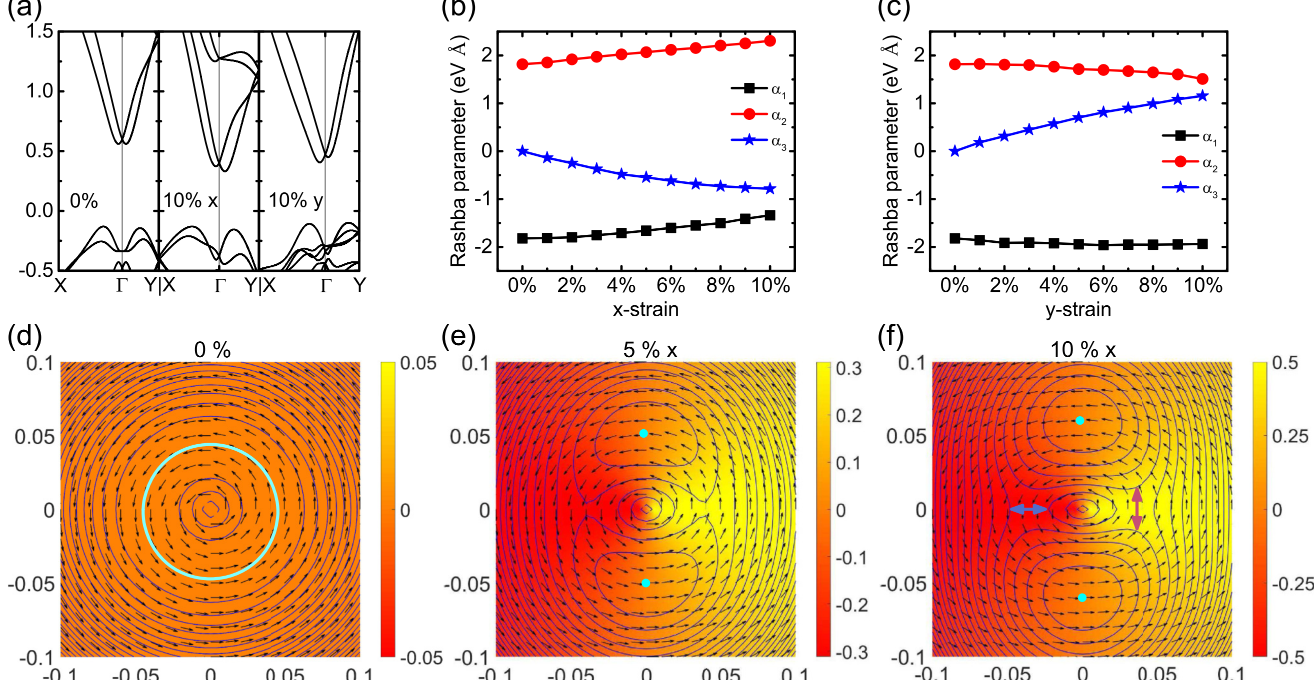

FIG. 2. (a) The energy bands of the monolayer with 0%, 10% x strain, or 10% y strain. (b), (c) The Rashba parameters (α_1, α_2, α_3) in Hamiltonian (1) for different x- or y-strain values. (d)–(f) The spin textures of the lowest Rashba band near the Γ point under 0%, 5%, or 10% x strains caused by uniaxial x stress, where the in-plane spin components are indicated as arrows and the out-of-plane spin components $\langle\sigma_z\rangle$ are presented with the color scale, and we show the region defined by $k_x = -0.1$ to 0.1 Å^{-1} and $k_y = -0.1$ to 0.1 Å^{-1} in the Brillouin zone. The contours of energy are shown by the blue lines and the energy minima are marked as the cyan circle or points. When the Fermi level moves upward from the conduction band edge, the Fermi line topology changes from the two Fermi pockets [as the vertical purple double arrow shows in (f)] to the lines shown by the horizontal blue double arrow in (f).

study [31] and experimental values [33]. When the tensile x strain reaches 10% (x stress 1.71 N/m), the conduction band minima along the k_y direction become much lower than those along the k_x direction, which means that the conduction bands near the Γ point become strongly anisotropic. As a result, the calculated Rashba splitting energy $\mathcal{E}_R$ and k-vector offset k_0 are equivalent to 27.5 meV and 0.035 Å^{-1} along the k_x direction, but they become 69.6 meV and 0.060 Å^{-1} along the k_y direction. When the tensile y stress 1.82 N/m (10% tensile strain) is applied, the evaluated parameters $\mathcal{E}_R$ and k_0 are 23.6 meV and 0.031 Å^{-1} along the k_y direction, but 67.7 meV and 0.060 Å^{-1} along the k_x direction. These results reveal that the uniaxial x (y) stress makes the lowest conduction bands around the Γ point become two minimum points along the $\pm k_y$ ($\pm k_x$) direction, leading to strong anisotropy in the Rashba bands.

When uniaxial stress is applied, rotational symmetry no longer exists in the stretched monolayer BiTeI, and only $\mathcal{M}_x$ mirror symmetry remains. Under the mirror transformation $\mathcal{M}_x : x \to -x$, $(k_x, k_y) \to (-k_x, k_y)$ and $(\sigma_x, \sigma_y, \sigma_z) \to (\sigma_x, -\sigma_y, -\sigma_z)$. Then we can construct the two-band Hamiltonian for the lowest conduction bands near the Γ point,

$$\hat{H} = \mathcal{E}_k + \alpha_1 k_x \sigma_y + \alpha_2 k_y \sigma_x + \alpha_3 k_x \sigma_z, \tag{1}$$

where $\mathcal{E}_k = \frac{\hbar^2}{2}(\frac{k_x^2}{m_x} + \frac{k_y^2}{m_y})$, and the crossing point of the two bands is located at $\mathcal{E}_k = 0$ on the Γ point. The three Rashba parameters α_1, α_2, and α_3 in the Hamiltonian (1) can be obtained through fitting the conduction bands of the strained monolayer, and the strain dependences of the resulting parameters for the x/y stress are shown in Figs. 2(b) and 2(c). It is interesting that α_3 is negative for the uniaxial x stress, but becomes positive for the uniaxial y stress. We can see that uniaxial stress allows the emergence of a term $k_x\sigma_z$ in the Hamiltonian. It is another physical phenomenon arising from structural symmetry $\mathcal{M}_x$. Considering the Rashba Hamiltonian with a rotational group, there is no σ_z term up to the third order of k when the symmetry obeys C_2, C_{2v}, C_4, and C_{4v} [39]. When the point symmetry is C_3 or C_{3v}, there is no σ_z term in the first order of k, but some σ_z terms in the third order of k are allowed, for example, the $(k_x^3 - 3k_x k_y^2)\sigma_z$ term [39,40]. Therefore, we can conclude that uniaxial stress removes the C_{3v} symmetry and thus leads to the emergence of the $k_x\sigma_z$ term, which allows an out-of-plane spin component.

The eigenvalues of the two-band Hamiltonian (1) can be written as

$$\mathcal{E}_k^\lambda = \mathcal{E}_k + \lambda\sqrt{(\alpha_1^2 + \alpha_3^2)k_x^2 + \alpha_2^2 k_y^2}, \tag{2}$$

where $\lambda = \pm 1$ refers to the two bands. It should be noted that $\mathcal{E}_k = 0$ means $\mathcal{E}_k^\lambda = 0$. We can obtain the spin expectation values at the momentum $\mathbf{k}$ near the Γ point,

$$\langle \mathbf{k}\lambda|\sigma_x|\mathbf{k}\lambda\rangle = \frac{\lambda\alpha_2 k_y}{\sqrt{(\alpha_1^2 + \alpha_3^2)k_x^2 + \alpha_2^2 k_y^2}}, \tag{3}$$

$$\langle \mathbf{k}\lambda|\sigma_y|\mathbf{k}\lambda\rangle = \frac{\lambda\alpha_1 k_x}{\sqrt{(\alpha_1^2 + \alpha_3^2)k_x^2 + \alpha_2^2 k_y^2}}, \tag{4}$$

$$\langle \mathbf{k}\lambda|\sigma_z|\mathbf{k}\lambda\rangle = \frac{\lambda\alpha_3 k_x}{\sqrt{(\alpha_1^2 + \alpha_3^2)k_x^2 + \alpha_2^2 k_y^2}}. \tag{5}$$

Expression (5) means that a spin z component emerges, in addition to the in-plane components. It is also indicated that the spin y and z components along the $k_x = 0$ line are zero, which is in agreement with our first-principles calculations. This phenomenon can be regarded as the result of $\mathcal{M}_x$ mirror symmetry. Our first-principles investigation about the spin texture of the lowest conduction band with 10% strain along both x and y axes shows that the out-of-plane spin component has an important effect.

Furthermore, we present both the spin textures and energy contours of the lower Rashba band ($\lambda = -1$) near the Γ point for 0%, 5%, and 10% x strain in Figs. 2(d)–2(f). When the Fermi level is shifted downward from the crossing point, the Fermi lines will finally become two separated closed curves, and even reduce to the two points for the conduction band edge. The change of the Fermi line topology makes a Lifshitz transition as shown in Fig. 2(f). For a very low electron concentration, there are two Fermi pockets near the two conduction band minima, respectively, and there is a strong anisotropy in the occupied states, as shown in Figs. 2(e) and 2(f).

B. Carrier charge and spin currents through the electric field

Now we address electric-field-induced transport phenomena in the stretched monolayer BiTeI in the presence of electron carriers, which can be achieved by charge transferring between van der Waals layers or electrostatic doping [41]. We suppose that the in-plane electric field is so weak and the electron concentration is so small that there is little change in the crystal structure and the lowest conduction bands of monolayer BiTeI. By remaining in the regime of low electron concentration, we can fix the Fermi level near the conduction band edge, as shown in Fig. 3, and thus the occupied electrons are located in the lower Rashba band in the neighborhood of the Γ points. When a small in-plane electric field $\mathbf{E}$ is applied, the relaxation time approximation for the Boltzmann equation of the distribution function f can be expressed as $-\frac{e\mathbf{E}}{\hbar} \cdot \frac{\partial f}{\partial \mathbf{k}} = -\frac{f - f_0}{\tau}$, where τ is the electron relaxation time and here the Hall effect is not taken into consideration [42,43]. As the response to the external electric field, the distribution function can be expanded as $f = f_0 + f_1 + f_2 + \cdots$, where f_0 is the distribution function of the system in the absence of $\mathbf{E}$, and $f_n = (\frac{e\tau}{\hbar}\mathbf{E} \cdot \frac{\partial}{\partial \mathbf{k}})^n f_0$ comes from the iterative substitution of the Boltzmann equation [42–45].

Consequently, the charge current $\mathbf{j}_c$ can be written as [42,43]

$$\mathbf{j}_c = -\frac{e\tau}{\hbar^2}\int d\mathbf{k}\,\delta(\mathcal{E}_k^\lambda - \mathcal{E}_F)(\mathbf{E} \cdot \nabla_k \mathcal{E}_k^\lambda)\nabla_k \mathcal{E}_k^\lambda, \tag{6}$$

where $\lambda = -1$. We can define a normalized charge current as the ratio of current magnitude to doped electron concentration to describe the current-production efficiency. When the electric field is applied along the x direction, the normalized charge current j_{cn} as a function of electron concentrations under 10% strain along the x/y directions are shown in Fig. 3(a). We can explain this phenomenon with the Drude model $j = ne^2\tau E/m^*$, where n is the concentration of doped electrons. When the Fermi level is shifted upward from the

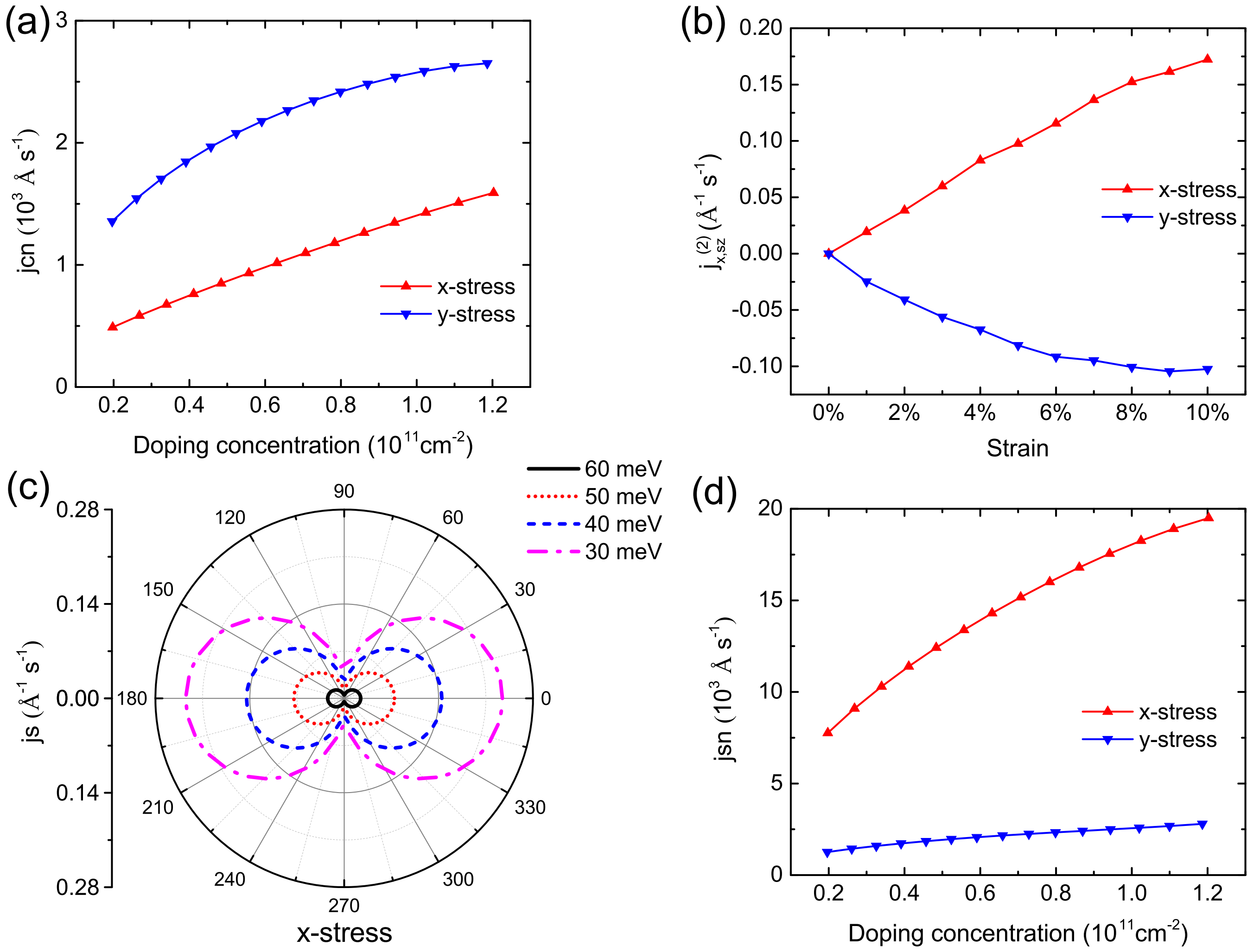

FIG. 3. (a) The normalized charge currents j_{cn} in $e\tau E/\hbar^2$ as functions of electron concentrations with 10% x strain or y strain. (b) The second-order spin currents $j^{(2)}_{x,s_z}$ in $e^2\tau^2E^2/\hbar^3$ under different x strain or y strain caused by uniaxial stress, where the Fermi level is 10 meV lower than the crossing point. (c) The spin currents j_s in $e^2\tau^2E^2/\hbar^3$ with 10% x strain, as functions of the θ angle, when the Fermi level is lower than the crossing point by 60, 50, 40, or 30 meV. The conduction band energy minima are lower than the crossing point by 69.6 meV for 10% x strain, or 67.7 meV for 10% y strain. (d) The normalized maximal spin currents j_{sn} in $e^2\tau^2E^2/\hbar^3$ as functions of electron concentrations under 10% x strain or y strain. The electric field is along the x direction in all the cases.

band edge, $\frac{\partial^2 E}{\partial k_x^2} = \frac{\hbar^2}{m_x} - (\alpha_1^2+\alpha_3^2)\alpha_2^2 k_y^2/[(\alpha_1^2+\alpha_3^2)k_x^2+\alpha_2^2 k_y^2]^{\frac{3}{2}}$ will be increasing, which reduces the m^* value in the system. Thus the normalized current in $e\tau E$ will be monotonically increasing in this circumstance.

As for the spin current, we take the conventional definition of the spin current operator as $\hat{J}_{\mu,s_\nu} = \frac{1}{4}\{\frac{\partial \hat{H}}{\partial k_\mu}, \sigma_\nu\}$, which refers to the spin component s_ν flowing along the μ direction [43,46,47]. It should be especially noted that this definition of the spin current operator will be invalid when the third-power k terms are included in the Hamiltonian [48]. Fortunately, the k terms in our Hamiltonian are only to the first order in the presence of a small electron concentration ($\mathcal{E}_F < 0$).

Then we obtain the three nonzero components of the spin current near the Γ point,

$$\langle \mathbf{k}\lambda|\hat{J}_{y,s_x}|\mathbf{k}\lambda\rangle = \frac{\lambda\hbar^2\alpha_2 k_y^2}{2m_y\sqrt{(\alpha_1^2+\alpha_3^2)k_x^2+\alpha_2^2k_y^2}} + \frac{\alpha_2}{2}, \quad (7)$$

$$\langle \mathbf{k}\lambda|\hat{J}_{x,s_y}|\mathbf{k}\lambda\rangle = \frac{\lambda\hbar^2\alpha_1 k_x^2}{2m_x\sqrt{(\alpha_1^2+\alpha_3^2)k_x^2+\alpha_2^2k_y^2}} + \frac{\alpha_1}{2}, \quad (8)$$

$$\langle \mathbf{k}\lambda|\hat{J}_{x,s_z}|\mathbf{k}\lambda\rangle = \frac{\lambda\hbar^2\alpha_3 k_x^2}{2m_x\sqrt{(\alpha_1^2+\alpha_3^2)k_x^2+\alpha_2^2k_y^2}} + \frac{\alpha_3}{2}. \quad (9)$$

For the isotropic Rashba model, we have $m_x = m_y$, $\alpha_1 = -\alpha_2$, and $\alpha_3 = 0$, and then derive $\langle \hat{J}_{y,s_x}\rangle = -\langle \hat{J}_{x,s_y}\rangle$, which is the same as Rashba's result [46]. The nonzero spin current expectation will not lead to the transport and accumulation of spin under the condition of thermodynamic equilibrium, and it can be connected to a non-Abelian SU(2) field generated by the spin-orbit coupling [49]. It can have real spin transport when the Rashba medium is constructed with a spatially modulated spin-orbit parameter [50,51]. For this reason, the zero-order spin current will not be addressed in the following.

It has been shown that odd (even) orders of the spin (charge) current become zero in the presence of time-reversal symmetry, and broken inversion symmetry allows the existence of nonzero even spin current [43]. Responding to the electric field, a second-order spin current occurs that can be defined by [43]

$$j^{(2)}_{\mu,s_\nu} = \int \frac{d^2\mathbf{k}}{(2\pi)^2}\langle \mathbf{k}\lambda|\hat{J}_{\mu,s_\nu}|\mathbf{k}\lambda\rangle f_2 \tag{10}$$

$$= \frac{e^2\tau^2}{4\pi^2\hbar^3}\int d\mathbf{k}\delta\big(\mathcal{E}^\lambda_k - \mathcal{E}_F\big)\big(\mathbf{E}\cdot\nabla_k\mathcal{E}^\lambda_k\big)\mathbf{E}\cdot\nabla_\mathbf{k}\langle\hat{J}_{\mu,s_\nu}\rangle. \tag{11}$$

When the electric field $\mathbf{E}$ is applied along the x or y direction, there are only three nonzero components for the spin current, $j^{(2)}_{x,s_y}$, $j^{(2)}_{x,s_z}$, and $j^{(2)}_{y,s_x}$. Returning to the isotropic Rashba system, our numerical calculations give that $j^{(2)}_{x,s_y} = 5j^{(2)}_{y,s_x}$ and $j^{(2)}_{x,s_z} = 0$ in the case of the x-direction electric field, which is in agreement with the spin current results of the isotropic Rashba model [43]. In Fig. 3(b), we present the spin current component $j^{(2)}_{x,s_z}$ under uniaxial stress (0%–10%) along the x/y direction when the Fermi level is 10 meV lower than the crossing point. When the x strain (y strain) reached 10%, the magnitude of $j^{(2)}_{x,s_z}$ is equivalent to $|j^{(2)}_{x,s_z}| \approx 0.6|j^{(2)}_{x,s_y}|$. It is clear that uniaxial stress leads to a remarkable spin s_z current $j^{(2)}_{x,s_z}$, in contrast to the isotropic case.

It is necessary to clarify the real-space distribution of the electrically generated spin current. The magnitude of the spin current along the θ direction ($\theta = 0$ means the x direction) is given by

$$\mathbf{j}_s = \sqrt{\big(j^{(2)}_{x,s_y} + j^{(2)}_{x,s_z}\big)^2\cos^2\theta + \big(j^{(2)}_{y,s_x}\big)^2\sin^2\theta}. \tag{12}$$

When the Fermi level is lower than the crossing point by 60, 50, 40, or 30 meV, our numerical results of the spin currents as functions of θ are shown in Fig. 3(c). The spin currents show giant anisotropy in the real space. They increase due to an enlarged electron concentration when the Fermi level moves upwards from the conduction band edge. To show the concentration dependence of the maximal spin currents per electron j_{sn}, we present in Fig. 3(d) the normalized maximal spin currents as functions of electron concentration for the two cases of the 10% strain along the x and y directions. Here, the definition of the normalized maximal spin currents is similar to that of the normalized charge current. Figure 3(d) indicates that the different orientations of uniaxial stress, even under the same electric field (along the x direction), will lead to very different normalized maximal spin currents.

The lifetime τ of electrons in the bulk BiTeI measured by experiment is 3.9×10^{-14} s [52] from the Dingle temperature in the Shubnikov–de Haas oscillations which have a strong Fermi energy dependence. When the Fermi level is 60 meV lower than the crossing point and the electric field is 1 V μm^{-1} along the x direction, we use the relaxation time τ of 3.9×10^{-14} s to estimate at this lifetime for convenience, and thus obtain that the ratio of the spin current to the charge current is equivalent to 0.09, and the spin current is 1.28×10^9 Å^{-1} s^{-1} for the 10% x strain.

TABLE I. The electron concentrations (cm^{-2}) for different Fermi levels ($\mathcal{E}_F$, defined with respect to the crossing point) in the presence of 5% and 10% x strains or y strains.

$\mathcal{E}_F$	−30 meV	−40 meV	−50 meV	−60 meV
5% x strain	1.03×10^{11}	5.1×10^{10}	1.2×10^{10}	
10% x strain	1.20×10^{11}	8.6×10^{10}	5.6×10^{10}	2.7×10^{10}
5% y strain	1.00×10^{11}	5.0×10^{10}	1.2×10^{10}	
10% y strain	1.02×10^{11}	7.3×10^{10}	4.6×10^{10}	2.0×10^{10}

C. Further discussions

It is noted that the spin-split Rashba states beyond the Rashba model can produce out-of-plane spin polarization without external stress [53]. The out-of-plane spin polarization was demonstrated in BiTeX (X = Cl, Br, I) compounds [15,18]. Such out-of-plane spin polarizations occur far from the Γ point, corresponding to the $(k_x^3 - 3k_xk_y^2)\sigma_z$ term in the Hamiltonian (coexisting with the hexagonal warping effect) [39]. In this work we keep the Fermi level lower than the crossing point of the two spin-split bands (it only needs a small electron concentration), so the occupied electrons are located near the Γ point. Thus the effective Hamiltonian is in the first order of k in this work. We show in Figs. 4(a)–4(c) the k distributions of the z component of the spin textures of the lowest conduction band in the Brillouin zone in the monolayer with 0%, 10% x strain, and 10% y strain obtained by first-principles calculations. The spin y and z components of the spin textures of the lowest conduction band along the $\Gamma \rightarrow X$ high-symmetry direction are also presented in Figs. 4(d)–4(f). From these results, it can be noted that the z component near the Γ point is remarkably enhanced by external uniaxial stress. Therefore, our work provides a way to mechanically manipulate out-of-plane spin polarization in such two-dimensional materials.

As for the realization of tensile strain on the 2D system, the commonly used polydimethylsiloxane (PDMS) substrate is found to transfer only 10% of the applied strain to the monolayer MoS_2 [54]. But the substrate with a beyond 1-GPa Young's modulus can effectively transfer 90% of the applied strain to the monolayer and thus the monolayer MoS_2 can reach ∼5% tensile strain [54]. Our first-principles calculations indicate that the elastic constants of monolayer BiTeI are C_{11} = 25.67 N/m and C_{22} = 25.59 N/m, which are close to those of a previous study (28.09 and 26.35 N/m) [38]. These are much lower than those of monolayer MoS_2 (131.33 and 131.45 N/m) [38]. As for the 2D Young's moduli, the calculated values of the monolayer BiTeI, 23.59 and 23.52 N/m, are also smaller than those of monolayer MoS_2 (123.27 and 123.38 N/m). Therefore, we believe that the giant uniaxial tensile stress on the monolayer BiTeI can be achieved in the experiment.

It is useful to show the relationship between the Fermi level and the electron concentration. In Table I we present the corresponding electron concentrations for the 5% and 10% strains when the Fermi level is lower than the crossing point by 30, 40, 50, and 60 meV. It should be noted that the conduction band edge is at −69.6 meV (with the crossing point defined as the zero energy) for 10% x strain (uniaxial stress

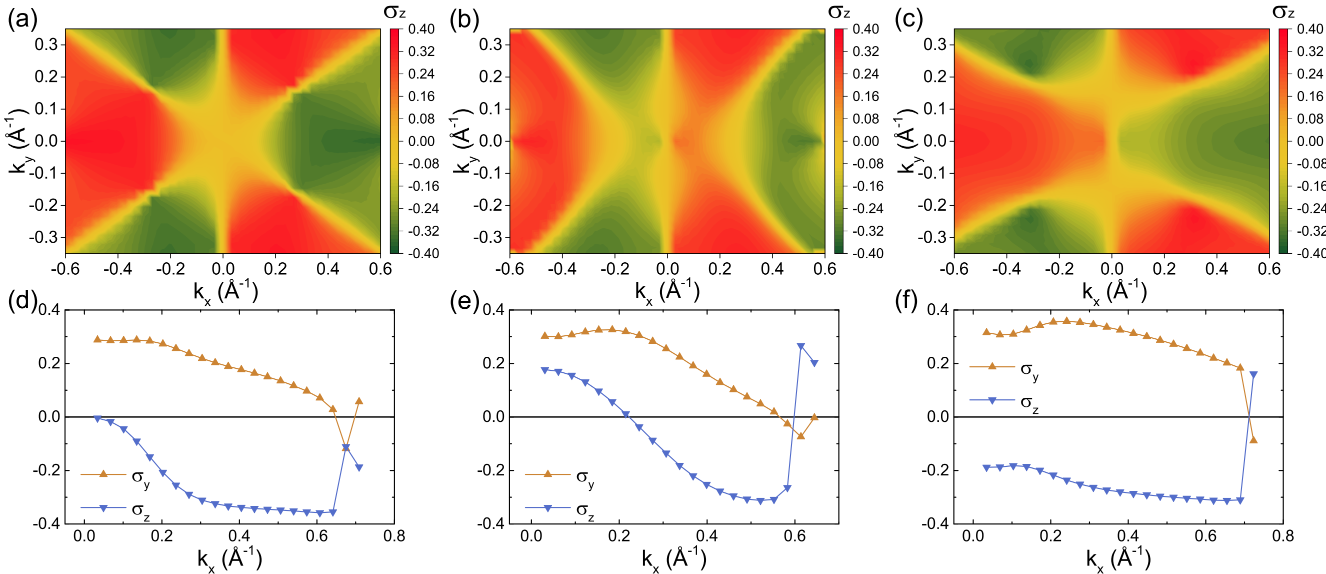

FIG. 4. The k distributions of the z component of spin textures of the lowest conduction band in the Brillouin zone in the monolayer with (a) 0%, (b) 10% x strain, and (c) 10% y strain. The y and z components of the spin textures of the lowest conduction band along the $\Gamma \rightarrow X$ high-symmetry direction in the monolayer with (d) 0%, (e) 10% x strain, and (f) 10% y strain are also shown. Here, the Γ point is located at $k_x = 0$, and the x component is zero along this high-symmetry line.

1.71 N/m), or at −67.7 meV for 10% y strain (uniaxial stress 1.82 N/m). For smaller stress, the conduction band edge moves toward the crossing point, and it becomes −53.2 meV for 5% x strain (uniaxial stress 0.99 N/m), or −53.4 meV for 5% y strain (uniaxial stress 1.05 N/m). Because a doped carrier concentration of 10^{13} cm^{-2} has been achieved by back-gate gating in transition-metal dichalcogenide monolayers [55,56] and 10^{14} cm^{-2} by ion liquid gating in graphene [57,58], the electron concentrations ranging from 0.12 to 1.20×10^{11} cm^{-2} should be experimentally accessible.

IV. CONCLUSION

In summary, we use uniaxial stress to manipulate the monolayer BiTeI semiconductor through first-principles calculations and theoretical analyses. Because uniaxial stress destroys C_{3v} symmetry, the monolayer has only $\mathcal{M}_x$ mirror symmetry, which allows the emergence of the $\alpha_3 k_x \sigma_z$ term in the effective model. We obtain an effective anisotropic Rashba Hamiltonian through fitting the Rashba bands with the lowest conduction bands near the Γ point up to a stress of 1.71 N/m for the x axis or 1.82 N/m for the y axis. We find the remarkable out-of-plane spin component in the stretched monolayer BiTeI, in addition to the usual in-plane spin components in the isotropic Rashba model. When electron carriers of low concentration are introduced into the monolayer, an in-plane electric field can induce the first-order charge current and second-order spin currents including an s_z spin current component increasing with uniaxial stress. Such electron carriers can be realized through electrostatic doping [41]. These make us believe that uniaxial stress and electric field together can open the door for controllable spintronic applications on the basis of 2D polar materials such as monolayer BiTeI.

ACKNOWLEDGMENTS

This work is supported by the Nature Science Foundation of China (No. 11574366 and No. 11974393), by the Strategic Priority Research Program of the Chinese Academy of Sciences (Grant No. XDB07000000), and by the Department of Science and Technology of China (Grant No. 2016YFA0300701). The calculations were performed in the supercomputer system at Institute of Physics and the Milky Way 2 supercomputer system at the National Supercomputer Center of Guangzhou, Guangzhou, China.

[1] E. I. Rashba and V. I. Sheka, Fiz. Tverd. Tela: Collected Papers **2**, 162 (1959).
[2] E. I. Rashba, Fiz. Tverd. Tela **2**, 1224 (1960).
[3] *Spin Physics in Semiconductors*, edited by M. I. Dyakonov, Springer Series in Solid-State Sciences Vol. 157 (Springer, Berlin, 2017).
[4] Y. A. Bychkov and É. I. Rashba, JETP Lett. **39**, 78 (1984).
[5] A. Manchon, H. C. Koo, J. Nitta, S. M. Frolov, and R. A. Duine, Nat. Mater. **14**, 871 (2015).
[6] T. Hu, F. Jia, G. Zhao, J. Wu, A. Stroppa, and W. Ren, Phys. Rev. B **97**, 235404 (2018).
[7] S. Singh and A. H. Romero, Phys. Rev. B **95**, 165444 (2017).
[8] J. Yuan, Y. Cai, L. Shen, Y. Xiao, J.-C. Ren, A. Wang, Y. P. Feng, and X. Yan, Nano Energy **52**, 163 (2018).
[9] A.-Y. Lu, H. Zhu, J. Xiao, C.-P. Chuu, Y. Han, M.-H. Chiu, C.-C. Cheng, C.-W. Yang, K.-H. Wei, Y. Yang, Y. Wang, D. Sokaras, D. Nordlund, P. Yang, D. A. Muller, M.-Y. Chou, X. Zhang, and L.-J. Li, Nat. Nanotechnol. **12**, 744 (2017).

[10] P. Z. Hanakata, A. S. Rodin, A. Carvalho, H. S. Park, D. K. Campbell, and A. H. Castro Neto, Phys. Rev. B **96**, 161401(R) (2017).
[11] P. Z. Hanakata, A. S. Rodin, H. S. Park, D. K. Campbell, and A. H. Castro Neto, Phys. Rev. B **97**, 235312 (2018).
[12] M. Noor-A-Alam, M. Lee, H.-J. Lee, K. Choi, and J. H. Lee, J. Phys.: Condens. Matter **30**, 385502 (2018).
[13] K. Premasiri, S. K. Radha, S. Sucharitakul, U. R. Kumar, R. Sankar, F.-C. Chou, Y.-T. Chen, and X. P. A. Gao, Nano Lett. **18**, 4403 (2018).
[14] Q. Zhang and U. Schwingenschlögl, Phys. Rev. B **97**, 155415 (2018).
[15] K. Ishizaka, M. S. Bahramy, H. Murakawa, M. Sakano, T. Shimojima, T. Sonobe, K. Koizumi, S. Shin, H. Miyahara, A. Kimura, K. Miyamoto, T. Okuda, H. Namatame, M. Taniguchi, R. Arita, N. Nagaosa, K. Kobayashi, Y. Murakami, R. Kumai, Y. Kaneko, Y. Onose, and Y. Tokura, Nat. Mater. **10**, 521 (2011).
[16] A. Crepaldi, L. Moreschini, G. Autès, C. Tournier-Colletta, S. Moser, N. Virk, H. Berger, P. Bugnon, Y. J. Chang, K. Kern, A. Bostwick, E. Rotenberg, O. V. Yazyev, and M. Grioni, Phys. Rev. Lett. **109**, 096803 (2012).
[17] G. Landolt, S. V. Eremeev, Y. M. Koroteev, B. Slomski, S. Muff, T. Neupert, M. Kobayashi, V. N. Strocov, T. Schmitt, Z. S. Aliev, M. B. Babanly, I. R. Amiraslanov, E. V. Chulkov, J. Osterwalder, and J. H. Dil, Phys. Rev. Lett. **109**, 116403 (2012).
[18] S. V. Eremeev, I. A. Nechaev, Y. M. Koroteev, P. M. Echenique, and E. V. Chulkov, Phys. Rev. Lett. **108**, 246802 (2012).
[19] M. Sakano, M. S. Bahramy, A. Katayama, T. Shimojima, H. Murakawa, Y. Kaneko, W. Malaeb, S. Shin, K. Ono, H. Kumigashira, R. Arita, N. Nagaosa, H. Y. Hwang, Y. Tokura, and K. Ishizaka, Phys. Rev. Lett. **110**, 107204 (2013).
[20] B. Monserrat and D. Vanderbilt, Phys. Rev. Mater. **1**, 054201 (2017).
[21] S. Bordács, J. G. Checkelsky, H. Murakawa, H. Y. Hwang, and Y. Tokura, Phys. Rev. Lett. **111**, 166403 (2013).
[22] M. Sakano, J. Miyawaki, A. Chainani, Y. Takata, T. Sonobe, T. Shimojima, M. Oura, S. Shin, M. S. Bahramy, R. Arita, N. Nagaosa, H. Murakawa, Y. Kaneko, Y. Tokura, and K. Ishizaka, Phys. Rev. B **86**, 085204 (2012).
[23] C. J. Butler, H.-H. Yang, J.-Y. Hong, S.-H. Hsu, R. Sankar, C.-I. Lu, H.-Y. Lu, K.-H. O. Yang, H.-W. Shiu, C.-H. Chen, C.-C. Kaun, G.-J. Shu, F.-C. Chou, and M.-T. Lin, Nat. Commun. **5**, 4066 (2014).
[24] Y. Kohsaka, M. Kanou, H. Takagi, T. Hanaguri, and T. Sasagawa, Phys. Rev. B **91**, 245312 (2015).
[25] J. S. Lee, G. A. H. Schober, M. S. Bahramy, H. Murakawa, Y. Onose, R. Arita, N. Nagaosa, and Y. Tokura, Phys. Rev. Lett. **107**, 117401 (2011).
[26] L. Demkó, G. A. H. Schober, V. Kocsis, M. S. Bahramy, H. Murakawa, J. S. Lee, I. Kézsmárki, R. Arita, N. Nagaosa, and Y. Tokura, Phys. Rev. Lett. **109**, 167401 (2012).
[27] M. S. Bahramy, B.-J. Yang, R. Arita, and N. Nagaosa, Nat. Commun. **3**, 679 (2012).
[28] S. V. Eremeev, I. A. Nechaev, and E. V. Chulkov, Phys. Rev. B **96**, 155309 (2017).
[29] J. I. Facio, D. Efremov, K. Koepernik, J.-S. You, I. Sodemann, and J. van den Brink, Phys. Rev. Lett. **121**, 246403 (2018).
[30] Y. Qi, W. Shi, P. G. Naumov, N. Kumar, R. Sankar, W. Schnelle, C. Shekhar, F.-C. Chou, C. Felser, B. Yan, and S. A. Medvedev, Adv. Mater. **29**, 1605965 (2017).
[31] Y. Ma, Y. Dai, W. Wei, X. Li, and B. Huang, Phys. Chem. Chem. Phys. **16**, 17603 (2014).
[32] N. L. Zaitsev, R. Tonner, and I. A. Nechaev, J. Phys.: Condens. Matter **31**, 204001 (2019).
[33] B. Fülöp, Z. Tajkov, J. Pető, P. Kun, J. Koltai, L. Oroszlány, E. Tóvári, H. Murakawa, Y. Tokura, S. Bordács *et al.*, 2D Mater. **5**, 031013 (2018).
[34] P. E. Blöchl, Phys. Rev. B **50**, 17953 (1994).
[35] G. Kresse and J. Hafner, Phys. Rev. B **47**, 558 (1993).
[36] J. P. Perdew, K. Burke, and M. Ernzerhof, Phys. Rev. Lett. **77**, 3865 (1996).
[37] H. J. Monkhorst and J. D. Pack, Phys. Rev. B **13**, 5188 (1976).
[38] S. Haastrup, M. Strange, M. Pandey, T. Deilmann, P. S. Schmidt, N. F. Hinsche, M. N. Gjerding, D. Torelli, P. M. Larsen, A. C. Riis-Jensen, J. Gath, K. W. Jacobsen, J. J. Mortensen, T. Olsen, and K. S. Thygesen, 2D Mater. **5**, 042002 (2018).
[39] S. Vajna, E. Simon, A. Szilva, K. Palotas, B. Ujfalussy, and L. Szunyogh, Phys. Rev. B **85**, 075404 (2012).
[40] L. Fu, Phys. Rev. Lett. **103**, 266801 (2009).
[41] P. V. Nguyen, N. C. Teutsch, N. P. Wilson, J. Kahn, X. Xia, A. J. Graham, V. Kandyba, A. Giampietri, A. Barinov, G. C. Constantinescu, N. Yeung, N. D. M. Hine, X. Xu, D. H. Cobden, and N. R. Wilson, Nature (London) **572**, 220 (2019).
[42] H. Yu, Y. Wu, G.-B. Liu, X. Xu, and W. Yao, Phys. Rev. Lett. **113**, 156603 (2014).
[43] K. Hamamoto, M. Ezawa, K. W. Kim, T. Morimoto, and N. Nagaosa, Phys. Rev. B **95**, 224430 (2017).
[44] I. Sodemann and L. Fu, Phys. Rev. Lett. **115**, 216806 (2015).
[45] T. Morimoto, S. Zhong, J. Orenstein, and J. E. Moore, Phys. Rev. B **94**, 245121 (2016).
[46] E. I. Rashba, Phys. Rev. B **68**, 241315(R) (2003).
[47] J. Sinova, D. Culcer, Q. Niu, N. A. Sinitsyn, T. Jungwirth, and A. H. MacDonald, Phys. Rev. Lett. **92**, 126603 (2004).
[48] H.-J. Drouhin, G. Fishman, and J.-E. Wegrowe, Phys. Rev. B **83**, 113307 (2011).
[49] I. V. Tokatly, Phys. Rev. Lett. **101**, 106601 (2008).
[50] E. B. Sonin, Phys. Rev. B **76**, 033306 (2007).
[51] Q.-F. Sun, X. C. Xie, and J. Wang, Phys. Rev. B **77**, 035327 (2008).
[52] C. Martin, E. D. Mun, H. Berger, V. S. Zapf, and D. B. Tanner, Phys. Rev. B **87**, 041104(R) (2013).
[53] C. R. Ast, J. Henk, A. Ernst, L. Moreschini, M. C. Falub, D. Pacilé, P. Bruno, K. Kern, and M. Grioni, Phys. Rev. Lett. **98**, 186807 (2007).
[54] Z. Liu, M. Amani, S. Najmaei, Q. Xu, X. Zou, W. Zhou, T. Yu, C. Qiu, A. G. Birdwell, F. J. Crowne *et al.*, Nat. Commun. **5**, 5246 (2014).
[55] K. F. Mak, K. He, C. Lee, G. H. Lee, J. Hone, T. F. Heinz, and J. Shan, Nat. Mater. **12**, 207 (2013).
[56] Y. Zhang, T. Oka, R. Suzuki, J. Ye, and Y. Iwasa, Science **344**, 725 (2014).
[57] D. K. Efetov and P. Kim, Phys. Rev. Lett. **105**, 256805 (2010).
[58] J. Ye, M. F. Craciun, M. Koshino, S. Russo, S. Inoue, H. Yuan, H. Shimotani, A. F. Morpurgo, and Y. Iwasa, Proc. Natl. Acad. Sci. USA **108**, 13002 (2011).